



# Characterizing warm atmospheric boundary layer over land by combining Raman and Doppler lidar measurements

YUFEI CHU,<sup>1,2</sup> ZHIEN WANG,<sup>1,2,\*</sup> LULIN XUE,<sup>3</sup> MIN DENG,<sup>2</sup> GUO LIN,<sup>1,2</sup> HAILING XIE,<sup>1,2</sup> HYEYUM HAILEY SHIN,<sup>3</sup> WEIWEI LI,<sup>3</sup> GRANT FIRL,<sup>3</sup> DANIEL F. D'AMICO,<sup>3</sup> DONG LIU,<sup>4</sup> AND YINGJIAN WANG<sup>4</sup>

<sup>1</sup>*Department of Atmospheric and Oceanic Sciences, University of Colorado Boulder, Boulder, Colorado, USA*

<sup>2</sup>*Laboratory for Atmospheric and Space Physics, Department of Atmospheric and Oceanic Sciences, University of Colorado Boulder, Boulder, Colorado, USA*

<sup>3</sup>*National Center for Atmospheric Research, Boulder, Colorado, USA*

<sup>4</sup>*University of Science and Technology of China, Hefei, China*

\*[Zhien.Wang@lasp.colorado.edu](mailto:Zhien.Wang@lasp.colorado.edu)

**Abstract:** PBL plays a critical role in the atmosphere by transferring heat, moisture, and momentum. The warm PBL has a distinct diurnal cycle including daytime convective mixing layer (ML) and nighttime residual layer developments. Thus, for PBL characterization and process study, simultaneous determinations of PBL height (PBLH) and ML height (MLH) are necessary. Here, new approaches are developed to provide reliable PBLH and MLH to characterize warm PBL evolution. The approaches use Raman lidar (RL) water vapor mixing ratio (WVMR) and Doppler lidar (DL) vertical velocity measurements at the Southern Great Plains (SGP) atmospheric observatory, which was established by the Atmospheric Radiation Measurement (ARM) user facility. Compared with widely used lidar aerosol measurements for PBLH, WVMR is a better trace for PBL vertical mixing. For PBLH, the approach classifies PBL water vapor structures into a few general patterns, then uses a slope method and dynamic threshold method to determine PBLH. For MLH, wavelet analysis is used to re-construct 2-D variance from DL vertical wind velocity measurements according to the turbulence eddy size to minimize the impacts of gravity wave and eddy size on variance calculations; then, a dynamic threshold method is used to determine MLH. Remotely-sensed PBLHs and MLHs are compared with radiosonde measurements based on the Richardson number method. Good agreements between them confirm that the proposed new algorithms are reliable for PBLH and MLH characterization. The algorithms are applied to warm seasons' RL and ML measurements at the SGP site for five years to study warm season PBL structure and processes. The weekly composited diurnal evolutions of PBLHs and MLHs in warm climate were provided to illustrate diurnal and seasonal PBL evolutions. This reliable PBLH and MLH dataset will be valuable for PBL process study, model evolution, and PBL parameterization improvement.

© 2022 Optica Publishing Group under the terms of the [Optica Open Access Publishing Agreement](#)

## 1. Introduction

The Atmospheric Boundary Layer (ABL) or Planetary Boundary Layer (PBL) is the lowest portion of the troposphere and is directly affected by the earth's surface. The response time to surface forcing (including friction, evaporation, heat conduction, and pollutant diffusion, etc.) is generally no more than one hour [1,2]. PBL depths vary in time and space ranging from the lowest several hundred meters to 3km or higher over mid-latitude land [1,3]. The clear-sky PBL has a distinct diurnal cycle corresponding to the solar radiation. After sunrise, solar surface heating drives the growth of a convective mixing layer (ML) with vigorous turbulence [4]. Near

sunset, turbulence decays, and the ML gradually transits to a stable residual layer during nighttime [5]. Although the ML responds to the vertical transport of energy and mass within the PBL, daytime ML developments are closely coupled with nighttime PBL properties [6,7]. Therefore, it is necessary to know both PBL and ML properties to characterize PBL evolution and impact [8,9]. In this article, we define the vertical distance from the ground to the bottom of capping inversion or top of the residual layer as PBL height (PBLH), and define the height from the ground to the top of the mixing layer as ML height (MLH). In general, ML is part of PBL (ML+residual layer) or the whole PBL [1,8,9].

PBL plays a critical role in the atmosphere because the surface heat, moisture, and momentum fluxes are transferred to the atmosphere above through the PBL. Multi-scale processes, including surface fluxes, radiation, dynamics, turbulence, cloud, and precipitation, control PBL evolutions [10–12]. The ability to represent PBL processes depends on understanding the underlying boundary-layer processes from observations [13–15]. Many PBL schemes were developed to represent the roles of turbulent eddies in PBL thermodynamic and kinematic structures [14,16–20]. Currently, there are over ten PBL schemes, mostly Turbulent Kinetic Energy (TKE) based or local K theory plus non-local effects. They are selectable within the advanced research version of the Weather Research and Forecasting (WRF) Model, indicative of the challenges in capturing turbulence impacts within PBL in models [12,14]. Considering the fundamental role of the PBL, the performance of models in simulating weather and air quality depends on the selections of the PBL scheme, as demonstrated in many modeling sensitivity studies [15,21].

Improving PBL parameterization requires an advanced understanding of processes controlling PBL and ML evolution over different time scales [22,23]. The Atmospheric Radiation Measurement (ARM) Southern Great Plains (SGP) site is the only site to offer multi-year routine surface flux and PBL structure observations, especially with observational enhancements since 2016. Here, Raman lidar (RL) and Doppler lidar (DL) measurements at the SGP site are used to characterize PBL structure and properties to support underlying PBL physical process studies [24–26]. To describe the diurnal cycle of PBL evolutions, we initially focus on quantifying PBLH and MLH reliably.

Many methods were developed for PBLH determinations with different limitations. The most widely used observations to detect the PBLH are in situ thermodynamic profiles from radiosonde [27], tethered balloon [28], aircraft [29]. PBLH determined by the Richardson number (RI) method from radiosonde measurements is often used as a reference for other detection methods [1–3,10]. However, these in situ measurements are temporally and spatially limited. Therefore, remote sensing data are widely explored for PBLH height determinations. Wind Profiling Radar [30] and Sodar [31] were used for PBLH detection, but their poor vertical resolution limits their application. Lidars can provide vertical profiles of aerosol, wind speed, water vapor, temperature at improved vertical resolutions [5–7,24,25,32]. Since the 1960s, various methods have been proposed to retrieve PBLH based on lidar aerosol measurements, including threshold methods [33,34], gradient methods [35], curve fitting [36,37], wavelet covariance [38], variance analysis [35,39], and machine learning [40]. Comparison studies of aerosol-based methods show that aerosol-based PBLHs performed well in general, but different approaches are often required to cover different conditions, especially over the land [6,7,10,25,41]. Vertical distributions of lidar aerosol signals are impacted by many factors, such as new particle formation and hygroscopic growth, other than vertical turbulence transport. Therefore, vertical distributions of water vapor profile could be a better trace to indicate PBL vertical mixing, especially between PBL and the free troposphere. Taniguchi [42] used water vapor mixing ratio (WVMR) data from Raman Lidar (RL) to determine PBLH, but the selections of thresholds affected the accuracy of the results. Thus, an improved PBLH determination with RL WVMR is needed.

The vertical structures of aerosol, vertical velocity variance, and potential temperature were used to determine MLHs with various algorithms and showed different performances [6,43,44].

Recently, many new methods based on aerosol data have been used to determine MLH, such as the minimum path algorithm based on the algorithm of graph theory [45], image edge detection method [46,47], supervised learning (AdaBoost algorithm), unsupervised learning (K-means, Expectation-Maximization) based on machine learning [48]. The aerosols within the residual layer impact MLH determinations with aerosols, especially in the morning and evening [9,42]. Since Taylor [49] showed that the vertical velocity variance is proportional to the intensity of turbulence, the variance of vertical velocity is widely used to study and for MLH determination. Near the daytime convective mixing-layer top, the vertical wind variance drops significantly, and this feature was used for MLH determinations with fixed threshold methods [44,49–53]. But different fixed variance thresholds are reported in the literature: Tucker et al. ( $0.04 \text{ m}^2\text{s}^{-2}$ ) [50], Pearson et al. ( $0.09 \text{ m}^2\text{s}^{-2}$ ) [51], Barlow et al. ( $0.1 \text{ m}^2\text{s}^{-2}$ ) [52], Vakkari et al. ( $0.1 \text{ m}^2\text{s}^{-2}$ ) [53] and Träumner et al. ( $0.16 \text{ m}^2\text{s}^{-2}$ ) [54]. These large ranges of thresholds indicate that the thresholds have to adjust under different conditions. Although Lenschow [43] provided a method for estimating the threshold based on the convection velocity, it was only valid for a well-developed convective boundary layer. The vertical velocity variance magnitudes also depend on the time window used for calculations [9,10,48] and turbulent eddy sizes [55]. Furthermore, the fixed variance threshold method cannot distinguish turbulence or gravity waves introduced variance [55]. The method using turbulence energy dissipation rates also has similar problems [56]. Therefore, a more robust MLH method is needed to process multi-year and multi-site measurements.

Here, we develop improved methods for PBLH and MLH using RL and DL measurements and applied them to multi-year warm-season observations at the SGP sites. For PBLH, the approach classifies PBL water vapor structures into a few general patterns, then uses a slope method and dynamic threshold method to determine PBLH. For MLH, wavelet analysis is used to calculate the variance of the vertical wind velocity according to turbulence eddy size by minimizing the impacts of other sources (e.g., gravity waves); then, a dynamic threshold method is used to determine MLH.

The paper is organized as follows: Section 2 describes the SGP site, instruments, and data. Section 3 introduces the method of obtaining the PBLH from WVMR data. In section 4, we discuss the algorithms for obtaining MLH. In section 5.1, these PBLH and MLH from DL and RL are compared with the sounding data. The diurnal evolution example of PBLH and MLH on a fair-weather day is discussed in section 5.2. The weekly average diurnal evolution of PBLH and MLH during the warm season is presented in section 5.3. Summary and conclusions are given in section 6.

## 2. Data

The SGP site is the longest operational U.S. Department of Energy (DOE) ARM site with multiple remote sensing capabilities [57,58]. In this study, we focus on simultaneous measurements of DL vertical velocity and RL WVMR together with four times daily radiosonde measurements. Table 1 shows the main parameters of RL and DL [59]. More detailed descriptions of the RL and DL can be found in the SGP RL handbook [60] and DL handbook [44].

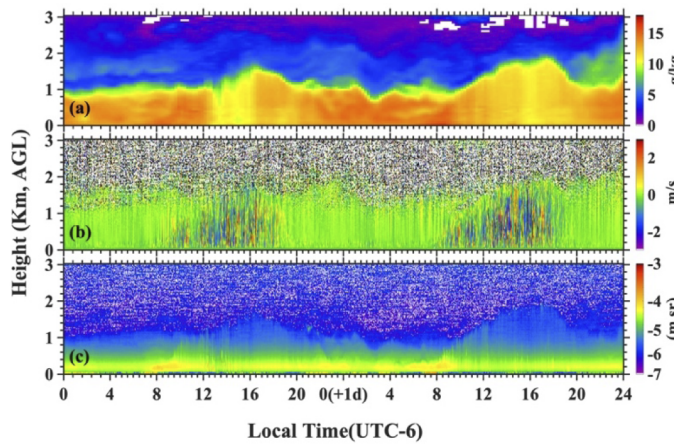
ARM archived RL and DL data streams used in this study are also listed in Table 1. Further noise reductions on these data are performed before PBLH and MLH detections. For WVMR, WVMR with values less than 0 g/kg or greater than 30 g/kg are eliminated, then a three-point (30-min) moving average is applied. For vertical wind velocity data, we first eliminate data with a signal-to-noise ratio less than -26 dB or an absolute value greater than 5 m/s. We then perform a five-point moving average along with a given height. If precipitation is reported in the surface meteorological data (sgpmetE13.b1), PBLH/MLH determinations will not be performed for the given period.

Figure 1 shows two continuous day measurements of low tropospheric WVMR (Fig. 1(a)), vertical velocity (Fig. 1(b)), and aerosol (Fig. 1(c)). The diurnal evolution of PBL structures is

**Table 1.** The specifications of Raman lidar and Doppler lidar at SGP [44,60].

Parameters	Raman Lidar	Doppler Lidar
<b>Data stream</b>	sgprlprofmr2news10mC1.c0	sgpdlfptc1.b1
<b>Vertical resolution</b>	60 m	30 m
<b>Temporal resolution</b>	10 min	~1.53 s (before 2018) ~3.06 s (after 2018)
<b>Laser</b>	Tripled Nd: YAG	Fiber laser
<b>Wavelength</b>	355 nm	1.5 $\mu$ m
<b>Pulse energy</b>	300-400 mJ	~100 $\mu$ J
<b>Pulse repetition frequency</b>	30 Hz	15 kHz

clearly illustrated by these measurements. DL vertical velocity measurements show that daily ML starts to develop around 8 am local time (LT) and reaches its peak around 4 pm each day. WVMR and aerosol structures show the corresponding daily vertical developments along with ML developments. WVMR indicates that nighttime PBL residual layer depths are slightly lower than 1 km, and daytime ML can grow much deeper than the residual layer. When ML top reaches the current PBL top, strong PBL top mixing could happen and result in WVMR decrease in PBL due to low WVMR in the free troposphere. Noticeable WVMR decreases between 1-4 pm on day one is due to the PBL top mixing that entrains the drier air from the free troposphere into the PBL. The impact of PBL top mixing is also noticeable on day two but is less significant than on day one. RL WVMR and DL aerosol structures show consistent PBL top height variations in this case. This example highlights that RL and DL offer complement measurements for PBLH and MLH determinations to characterize PBL evolution.



**Fig. 1.** Diurnal evolution of the PBL at SGP on May 27 to 28, 2018: (a) WVMR from Raman lidar, (b) vertical wind velocity from Doppler lidar, (c) aerosol backscattering coefficients from Doppler lidar.

### 3. PBL height determination with Raman lidar water vapor measurements

As illustrated in Fig. 1(a), water vapor is a good trace for PBL mixing processes, thus can be used for reliable PBLH determination [42]. As summarized in the flowchart given in Fig. 2, this new algorithm uses both slopes and dynamic thresholds to determine the PBLH from RL WVMR

according to different water vapor vertical patterns, which is governed by the PBL stability [1]. The key steps listed in the flowchart are summarized below.

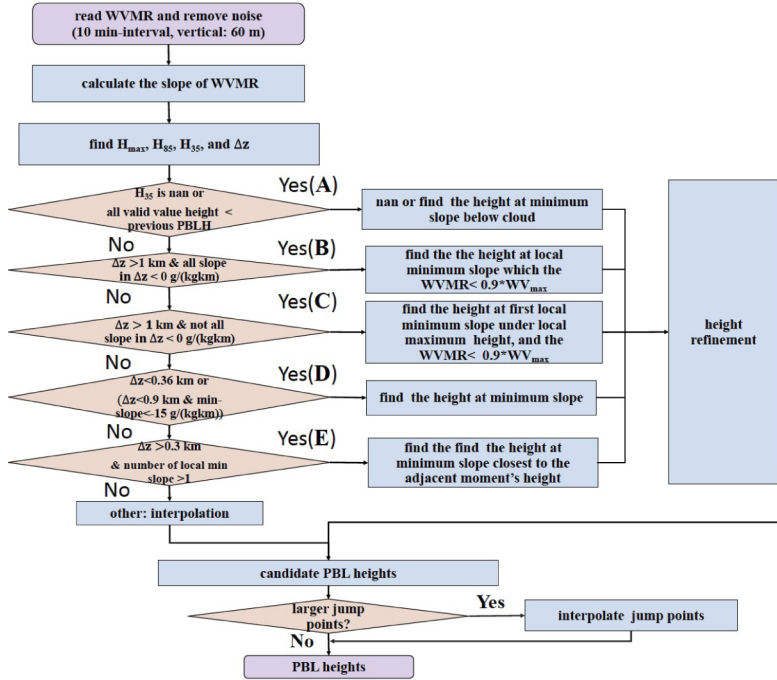


**Fig. 2.** The flowchart for PBLH determination. (WV<sub>max</sub>: maximum WVMR value above 0.2 km AGL, H<sub>max</sub>: the height of WV<sub>max</sub> above 0.2 km AGL, H<sub>85</sub>: the height of 0.85\* WV<sub>max</sub> above H<sub>max</sub>, H<sub>35</sub>: the height of 0.35\* WV<sub>max</sub> above H<sub>max</sub>, Δz : distance between H<sub>35</sub> and H<sub>85</sub>, nan: this profile is invalid)

**Step one: Data quality control and slope calculations.** We first determine the useful data height range for each profile based on WVMR errors provided in the data stream. As the vertical height increases, the WVMR error also increases gradually. The WVMR error is generally less than 10% within the boundary layer and increases rapidly above the PBL top. In the presence of optically thick low-level clouds, Raman lidar signals are quickly attenuated leading to high WVMR errors. The upper useful height range is determined at where WVMR error is over 20% or 1.5 g/kg for PBLH determination. Then, WVMR slopes are calculated by fitting five-point data to a linear function with the least-squares method. Local slope minimum are at where with 3 continuously reduced slopes below and followed by 2 continuously increased slopes, and need to be less than -1 g/(kg km).

**Step two: Vertical structure characterization.** Low tropospheric water vapor structures are often more complex than the case presented in Fig. 1 and require a different approach. Three WVMR levels are defined for water vapor structure pattern identifications. The first one is the maximum WVMR height (H<sub>max</sub>) above 0.2 km AGL (above ground level). Then, from H<sub>max</sub> upward, heights where WVMR first decreases below 85% and 35% of the maximum WVMR (H<sub>85</sub> and H<sub>35</sub>) are identified. Finally, the distance (Δz) is the height between H<sub>85</sub> and H<sub>35</sub>. The profile will be skipped if any of these heights are due to measurement issues associated with low clouds and precipitation. The purpose of using H<sub>35</sub> and H<sub>85</sub> is to measure how fast water vapor decrease from the PBL to the free troposphere to support the classification of PBL vertical structures. 85% and 35% of peak WVMR are good indicators for the lower PBL and free tropospheric WVMR

statistically. Uncertainties in WVMR have minor impacts on  $H_{35}$  and  $H_{85}$ , thus on PBL pattern identifications.  $H_{35}$  and  $H_{85}$  have no direct impacts on the measurement errors in PBLH.

**Step three:** PBLH determination according to WVMR structure patterns and its slope information:

A. Cloudy condition: RL can pass through some optically thin clouds or provide measurements between scattered clouds. However, in the presence of optically thick low clouds, RL can't provide a complete PBL water vapor structure. When the  $H_{35}$  is not identified or all WVMR are invalid within lower 1 km, this cloudy profile will not be processed. If all values above 1km are invalid values, or the maximum height of the valid value is lower than the PBLH at the previous processing time by 300 m, this profile will also not be processed. Except for 55 days without Raman lidar data and 44 days of precipitation, this situation accounts for about 77 days of the samples from the selected warm season.

When the maximum height of the effective value is within 300 m of the adjacent PBLH, the algorithm finds the adjacent local minimum slope's height below the first invalid height as the candidate PBLH. If the difference between this height and the PBLH at the previous processing time exceeds 500 m, the algorithm uses the height below the first invalid height as the candidate PBLH. This situation accounts for about 3.6% of the samples.

B. Stable boundary layer: As illustrated in Fig.3a, one common PBL structure is stable condition as indicated by slightly increase of potential temperature with height and capped by a weak temperature inversion. Under this thermodynamic condition, WVMR decreases almost linearly with height to 1km to 3 km starting from a few hundred meters above the ground, and the slopes of WVMR are almost negative. This pattern can be identified when  $\Delta z > 1\text{ km}$ , and all slopes within  $\Delta z$  are less than  $0 \text{ g}/(\text{kg km})$ , or  $\Delta z > 1.5 \text{ km}$ , and all slopes within  $\Delta z$  are less than  $0.5 \text{ g}/(\text{kg km})$ . This situation generally happens in nocturnal PBLs and accounts for about 20.7% of the samples during the study period. Under this condition, the first local minimum slope height above  $H_{\max}$  with WVMR less than the 90% of  $\text{WV}_{\max}$  is selected as candidate PBLH.

C. Multi-layer WVMR structure: Under synoptic weather conditions, horizontal water vapor advection can create a multi-layer structure. As illustrated in Fig. 3(b), WVMR gradually decreases from the ground, reaches a local minimum, and then rebounds. This pattern can be identified when  $\Delta z > 1\text{ km}$ , but not all slopes within  $\Delta z < 0 \text{ g}/(\text{kg km})$ , or  $\Delta z > 1.5 \text{ km}$ , and not all slopes within  $\Delta z < 0.5 \text{ g}/(\text{kg km})$ . This situation accounts for about 48.5% of the measurements.

For this multi-layer pattern, candidate PBLH will be determined based on upper layer WVMR magnitudes. If the WVMR of the upper layer only increases slightly, i.e., less than 500 m, candidate PBLH is determined the same way as the pattern B. On the other hand, if the WVMR increase is considerable, even close to the ground as given in Fig.3b, candidate PBLH will be set at the local maximum negative slope below the peak of the second layer.

D. Well-mixed PBL: Under a clear sunny day, PBL could be well mixed and capped by a strong temperature inversion as illustrated in Fig. 3(c). This pattern can be identified with  $\Delta z < 360 \text{ m}$  and slopes less than  $-4\text{g}/(\text{kg km})$  or with a strong local minimum of negative slope (generally less than  $-15\text{g}/(\text{kg km})$ ) which is five times stronger than local negative slope minimums in other conditions. The height of the strongest local negative slope minimum will be set as the candidate PBLH. This situation accounts for about 13.2% of the measurements.

E. A de-coupled layer: As illustrated in Fig.3d, the potential temperature profile has two well-mixed layers separated with a weak temperature inversion. Correspondingly, there are

two well-mixed WVVMR layers. This pattern is common over land when the mixing layer is shallower than the previous day's residual layer and over the ocean when PBL deepens and decouples. This pattern can be identified if there are two or more similar local minimums of WVVMR slope. This situation accounts for about 6.9% of the measurements.

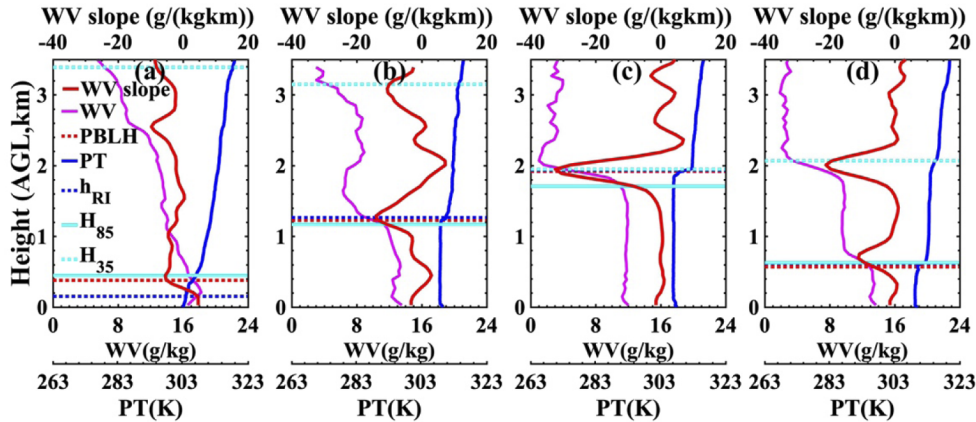


**Fig. 3.** Comparison of various algorithms with WVVMR data: (a) stable boundary layer(20180611,23:30); (b) multi-layer WVVMR structure(20170707,11:30); (c) well-mixed PBL(20180724,11:30); (d) de-couple layer(20180628,11:30); (WV: the vertical profile of WVVMR; WV slope: WV's slope; PBLH: the PBL height obtained by the WVVMR; PT: the vertical profile of the potential temperature;  $h_{RI}$ : the PBLH obtained when the RI = 0.25 from sounding data;  $H_{85}$ : the height of 85% of the maximum WVVMR;  $H_{35}$ : the height of 35% of the maximum WVVMR; all times are local time: UTC-6h).

For this pattern, the heights of the corresponding two largest local minimums of negative slopes are determined. If all slopes between the two heights are less than  $-3 \text{ g}/(\text{kg km})$ , the lower height is selected as the candidate PBLH. Otherwise, the local minimum slope height closing to the preceding one is selected as the candidate PBLH.

Other cases: When water vapor profiles do not fit with any above five patterns, PBLHs identified from the profiles at the nearby processing times will be interpolated to represent this time, considering that PBLH varies with time slowly. This situation accounts for about 7.1% of the measurements.

**Step four:** Candidate PBLHs determined above will be refined to provide a consistent PBL height according to potential temperature (PT) inversion layers. As indicated in Figs. 3(b) and 3(d), local slope minimums could be in the middle of PT inversion layers rather than near the base of PT inversion layer, which indicates that candidate PBLHs are biased higher. The locations of local WVVMR slope minimums could be impacted by free tropospheric water vapors and entrainment mixing. With PT profiles as guidance, a simple adjustment approach is implemented to adjust candidate PBLHs downward by 30 m if the slope  $< -20 \text{ g}/(\text{kg km})$ , 60 m if the slope  $< -10 \text{ g}/(\text{kg km})$ , and 120 m for others.

**Last:** We perform a consistent check of candidate PBLHs for each day based on the fact that PBLH changes gradually with time. If the values of consecutive three points (or less than three) are 500 m higher or lower than the preceding and following points, these points are more significant jump points. These values will be replaced with the interpolated values of the preceding and following values. After passing this check, PBLHs are finalized.

The algorithm provides consistent results from the sounding data as illustrated in Fig. 3. Figs. 3(b-d) show that the differences between WVVMR derived PBLHs and the RI method heights ( $h_{RI}$ ) are close to each other. But under stable boundary layer situations (see Fig.3a),  $h_{RI}$ , which

represents MLH, could be significantly lower than WVMR derived PBLH, which includes the residual layer.

#### 4. MLH from Doppler lidar vertical wind data

To determine MLHs accurately under different conditions routinely, we develop a wavelet-based approach to calculate the selected-scale variance from the DL vertical velocity data and minimize the impacts of gravity waves and eddies at different scales. Then, a dynamical threshold method is used to determine MLH from the variance. Figure 4 shows the flowchart of the algorithm.

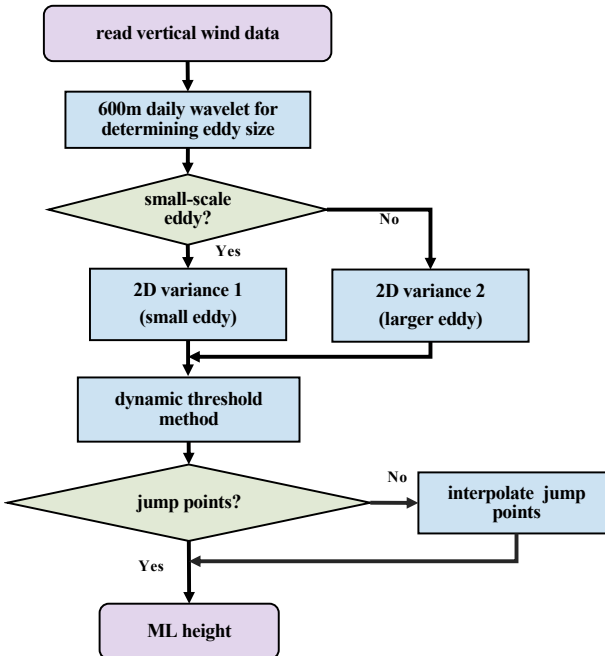


**Fig. 4.** The flowchart for MLH determination. (2D: Time dimension and height dimension)

**Step one:** After removing noise, the power spectral densities of wavelet analysis with DL vertical velocity measurements between 550~650 m are used to determine whether large or small eddies are presented for this day.

**Step two:** Different spectral ranges will be selected to construct 2-D (time and vertical height) variance based on the wavelet analysis discussed below based on the eddy size determination.

**Step three:** A dynamic threshold method is used to find MLH from the 2-D variance.

**Last:** A consistent check will be performed the same as PBLH determination.

##### 4.1. 2D variance determinations

###### 4.1.1. Eddy size

We use the wavelet method to distinguish eddy sizes to provide the energy distribution at different frequencies (scales) for a given day. Furthermore, each time scale is directly comparable to the other because of the normalization. Christopher and Gilbert [61] give a detailed discussion on the wavelet method.

Here three days (Figs. 5(a)-(c)) with different eddy scales based on ground-based fixed-site DL measurements are selected to illustrate the approach. It is clear that turbulent eddies in Fig. 5(c) last longer than eddies in Figs. 5(a)-(b). To capture characteristic features of the most energetic

turbulence eddies in daily MLs and avoid the influence of the small eddies near the ground, vertical velocities within 550~650 m AGL can be used for analysis at the SGP site, and results at 645m are presented below. DL measurements in the periods of two hours of the previous day and the next day are added to construct a vertical velocity time series to avoid the edge effect for wavelet analysis. Since the temporal resolutions of the data before and after 2018 are different, the temporal resolutions of DL measurements were coarsened with 5-point and 3-point averages for data before and after 2018. Then, the standard deviation and mean of the vertical velocity time series are calculated. The standard deviation normalizes the mean-removed time series to perform the wavelet transform using the MORLET wavelet base. Power spectra of temporal scales ranging from  $\sim 0.0025$ -hour up to  $\sim 0.5$ -hour are presented in Figs. 5(d)-(f).

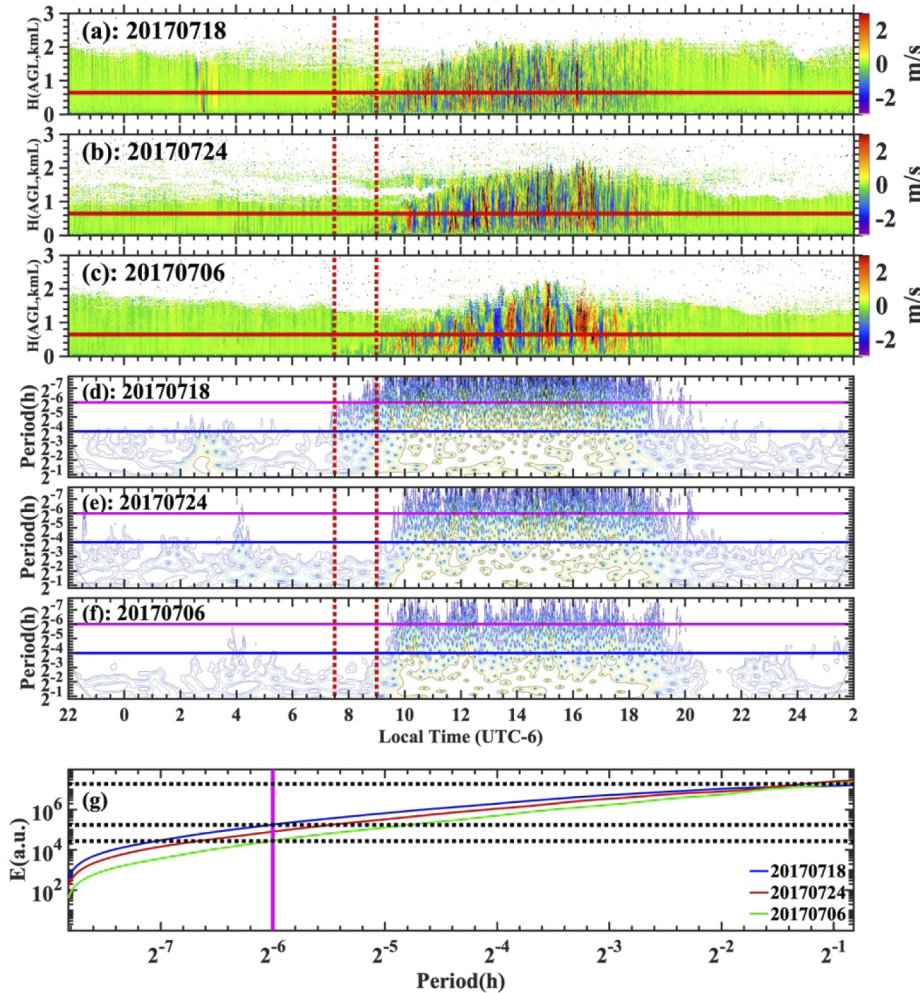


**Fig. 5.** Wavelet eddy size analysis: DL vertical velocity measurements: (a) July 18, 2017, (b) July 24, 2017, and (c) July 06, 2017 (horizontal red line: 645m); (d)~(f) wavelet power spectrums from (a)~(c) at 645m (magenta line: $2^{-6}$ , blue line: $2^{-4}$ , between the two vertical red dotted lines is 07:30 to 09:00, showing the time scale distribution of different turbulence magnitudes); (g) comparison of accumulated energy as periods (blue line: small eddy day, green line: larger eddy day).

The day dominated with small eddies (Fig. 5(d)) has higher energy intensity within  $2^{-6}$  hour (above the horizontal magenta line) than the day dominated by large eddies (Fig. 5(e)). In addition, it is clear that there is no energy distributed below  $2^{-4}$  hour during the nighttime.

To determine whether large size eddy dominates in daytime, we first integrate power spectrum between 06:00 to 18:00 local time, and then calculated accumulated energy distributions from small to large temporal scales with results shown in Fig. 5(g). Comparing the green and blue lines in Fig. 5(g), the contributions of eddies smaller than  $2^{-6}$  hours are clearly different. But total energy integral energy up to 0.5 hours are almost the same. Therefore, we can distinguish the eddy size of a whole day by comparing the ratio of the integrated energy values for temporal scales less than  $2^{-6}$  hours and less than  $2^{-1}$  hours during the daytime (06:00~18:00). We found that large eddy occurrence could be identified if the ratio is less than 1/200.

Wavelet analysis also allows us to select proper temporal scales for variance calculations to avoid the impact of gravity waves. There are gravity waves around 07:30~09:00 above the mixing layer in Fig. 5(a), which can be identified with energy detected within  $2^{-6} \sim 2^{-4}$  hours in Fig. 5(d) as compared to the days with no gravity waves during the same period in Fig. 5(e) and (f). The time scale of gravity waves is generally larger than  $2^{-6}$  hours. For example, gravity wave around 03:00 in Fig. 5(a) have energy in time scales between  $2^{-4} \sim 2^{-1}$  hours displayed in Fig. 5(d). Thus, we can avoid the effects of gravity waves by choosing a time scale of less than  $2^{-6}$  hours.

#### 4.1.2. 2-D variance construction

As demonstrated above, wavelet analysis results offer information to identify dominant eddy size and minimize the impact of the gravity wave on variance calculation. Thus, we use wavelet analysis results to construct 2-D variance by selecting short time period energy signals. Figure 6 presents an example. We perform wavelet analysis for each height based on DL observed 2-D vertical velocities. Power spectrum distributions (Fig. 6(c)) show strong turbulence during the daytime. Rather than using the whole spectrum to calculate variance as normally done, variances are calculated by integrating energy up to a selected period depending on the dominated eddy size determined above. For days with small eddies,  $2^{-6}$  hours is the upper integration limit, which can exclude the contribution of gravity wave. For days with large eddies, the upper integration limit is increased up to  $2^{-4}$  hours because the energy less than  $2^{-6}$  hour is very low under this condition. Although this increases the likelihood of including gravity wave contributions, we found that the co-occurrence of large eddies and gravity waves is low. The variance for selected height is given in Fig. 6(d).

By applying the approach to all heights, 2-D variance can be reconstructed at high temporal resolutions. Then, a 30-min moving averaging is applied to the high-frequency data. The final variance data is saved at 15-min time intervals, as displayed in Fig. 6(e).

The traditional variances of a 30-min time window at 15-min intervals are shown in Fig. 6(f) for comparison. It is clear that the traditional approach picked up gravity wave contributions during 2-4 and 10-12 hours. The proposed approach can significantly minimize the gravity wave contributions.

#### 4.2. Dynamic threshold method

A dynamic threshold method is introduced to cover a wide range of turbulence intensity, therefore overcome the fixed threshold method's deficiencies. The dynamic threshold is a method that dynamically adjusts the threshold's values for identifying the upper boundary of convective mixing layer based on the maximum turbulence intensity (variance) of the vertical profile at a certain moment. Although turbulence intensities decrease from a peak value BL to near zero above the ML, the magnitudes vary temporally. Thus, a single fixed threshold tends to cause MLH to be too low under weak turbulence and too high under strong turbulence. Implementing a dynamic threshold can better handle turbulence intensity variations. The several values are given

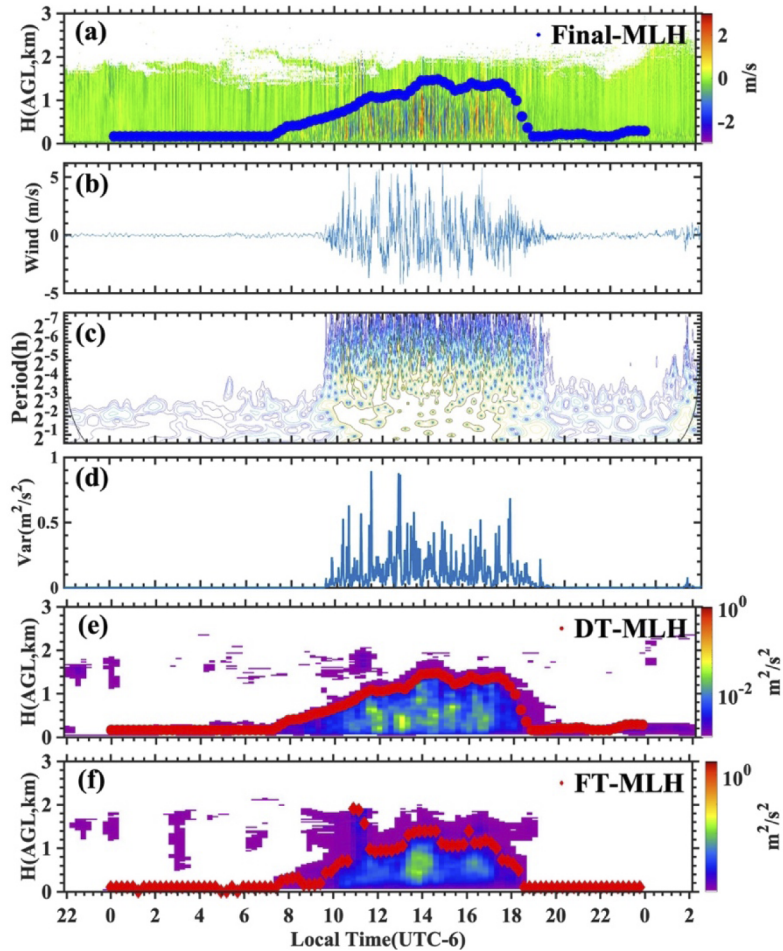


**Fig. 6.** An example of 2-D variance construction on July 2, 2018. (a) Measurements of DL vertical velocity after noise removal, (b) vertical velocity at 585m height, c) the wavelet power spectrum for (b), d) wavelet variance energy integrated up to less than 0.02 hours, (e) 2-D variance distribution by applying wavelet analysis to each measurement level, (f) normal variance of vertical velocities based on 30-min time window. FT-MLH: MLH obtained by the Fixed Threshold method; DT-MLH: MLH obtained by the Dynamic threshold method and Wavelet Var, Final-MLH: DT-MLH after the consistent check.

in Fig. 7, 0.055, 0.015, 0.1, these are empirical values from multi-year data at warm seasons. They are applicable on a clear day. According to experience, if the maximum variance is higher than  $0.55 \text{ m}^2/\text{s}^2$ , the threshold is set as  $0.055 \text{ m}^2/\text{s}^2$ . if the maximum variance is less than  $0.1 \text{ m}^2/\text{s}^2$ , the threshold is set as  $0.015 \text{ m}^2/\text{s}^2$ . For maximum variance between  $0.1 \text{ m}^2/\text{s}^2$  and  $0.55 \text{ m}^2/\text{s}^2$ , the threshold increases linearly from a minimum of  $0.015 \text{ m}^2/\text{s}^2$  to a maximum of  $0.055 \text{ m}^2/\text{s}^2$ . To determine MLH, we search upwards from the height of the maximum variance. The first height where the variance value decreases below the dynamic threshold is set as MLH.

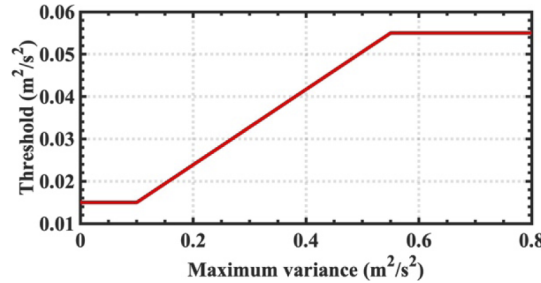


**Fig. 7.** The relationship between dynamic thresholds and maximum variances.

Figure 8 provides a comparison of MLHs derived from traditional variances with the fixed-threshold method (FT-MLH) and wavelet reconstructed approach with the dynamical threshold approach (DT-MLH) for six selected profiles. The results from the two approaches could be very close for profiles in Figs. 8(a)-(b). But results of the two approaches could differ significantly in other cases. With small variances due to weak turbulence or large eddies, FT-MLHs could

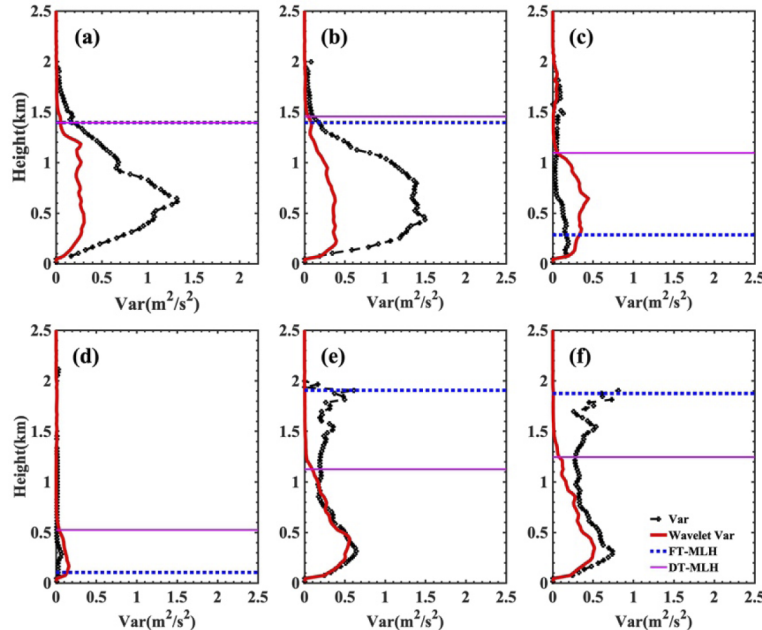


**Fig. 8.** Comparison of MLHs calculated by the fixed threshold method with the traditional variance (Var) based on DL vertical velocity and the dynamical threshold method with wavelet constructed variances (Wavelet Var): a) 16:00, b) 15:30, c) 10:30, d) 08:45, e) 11:00, and f) 11:15 On July 2, 2018 (LT).

be biased low (Figs. 8(c)-(d)). When there are gravity wave activities above the mixing layer, the traditional variance calculations could pick up gravity wave contributions to extend high variance above the mixing layer to overestimate MLHs. FT-MLHs and DT-MLHs for the whole day are presented in Fig. 6(e)-(f). The difference between them are clear. Final MLHs, which are DT-MLHs after the consistent check are the same as DT-MLHs for this case because there are no sharp jumps in DT-MLHs, over plotted in Fig. 6(a) clearly show that MLHs track the ML top well.

## 5. Evaluation and results

Here, the sounding data results with the RI method [1–3,10] are compared with PBLHs and MLHs described above. An example of diurnal PBLH and MLH variation is discussed. The approaches are applied to five-year RL and DL measurements at the SGP site together to characterize PBL/ML evolution. Composite weekly average diurnal variations of the PBLH and MLH during the warm season are provided to illustrate seasonal PBL and ML evolutions.

### 5.1. Comparison with radiosonde measurements

At the SGP site, radiosondes are regularly launched four times daily around 05:30, 11:30, 17:30, and 23:30 (local time). However, they could do up to eight times per day during intensive observation periods, which offers a great opportunity to evaluate lidar derived PBLHs and MLHs. The PBL depths from the Richardson method [27,62] ( $h_{RI}$ ) with radiosonde data are normally the same as the mixing layer depth during the day. The RI method determines that the ML height is the height of RI greater than the critical value (0.25), where RI is defined as:

$$RI = \frac{gz(\theta(z) - \theta(s))}{\theta(s)[(u(z) - u(s))^2 + (v(z) - v(s))^2]}. \quad (1)$$

Where  $g$  is gravitational acceleration,  $s$  is the near-ground position,  $z$  is detection position above ground,  $\theta$  is the potential temperature, and  $u$  and  $v$  are horizontal wind speeds. The RI method is not very dependent on the vertical resolution of the sounding data. Therefore, this paper uses the RI method as a contrast height between the PBL height assessment based on Raman lidar and the ML height assessment based on Doppler lidar.

Therefore, we can use radiosonde results from sunrise to 18:00 for MLH evaluations and from 11:30 to sunset for PBLH evaluations when ML is fully developed to reach the PBL top. This study only focuses on the warm season PBL from May 1st to October 1st. Observations during precipitation events are excluded from the comparison.

Figure 9 shows PBLH and MLH comparison results. The WVMR derived PBLHs agree with  $h_{RI}$  well based on 513 collocated measurements. The mean bias is -30 m, the RMSE (Root Mean Square Error) is 313 m, and the R (linear Regression) is 0.81. As expected, the agreement between DL vertical velocity derived MLHs with  $h_{RI}$  is better than PBLH because  $h_{RI}$  is a better indicator for MLH than PBLH. As shown in Fig. 9(b), the bias is 8 m, the RMSE is 264 m, and the R is 0.90.

However, there are points with large differences (could be more than 1.5 km). Several reasons could attribute to these differences:

First, the sounding balloon may drift far away from the ground station as it ascends. Although the horizontal drifts of radiosonde balloons during their ascent are generally small and negligible [63], they could be significant under synoptic weather events. Radiosonde could drift into clouds even though it could be clear at the SGP site.

Second, although the RI method is often used as the truth for remotely sensed PBLH and MLH, results from the RI method are also subject to uncertainties, especially associated with selecting ground parameters [1,64]. In Fig. 9(b), there are few points with  $h_{RI}$  higher than MLH

by more than 0.5 km. These samples are in the morning during the mixing layer deepening, and  $h_{RI}$  is the same as PBLH, but the convective plume is way shallower than PBL top.

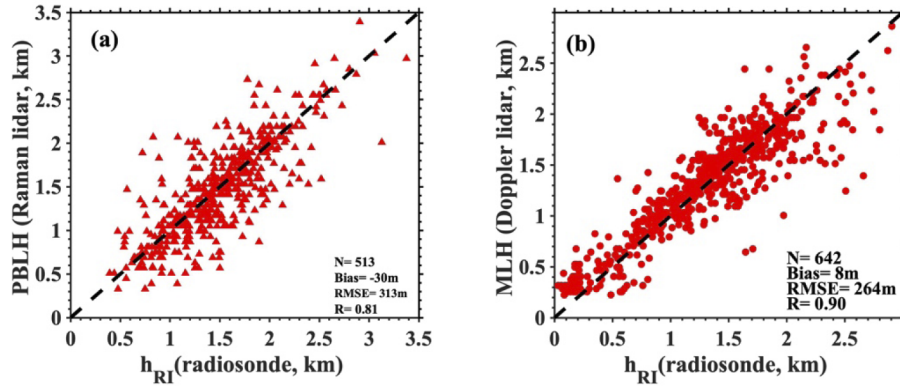


**Fig. 9.** Comparison of Raman lidar PBLHs (a) and Doppler lidar MLHs with radiosonde measurements during the warm season from 2016 to 2020. (N: sample number, Bias: deviation of the averages of two height; RMSE: root mean square error, and R: linear correlation coefficient.)

Third, RL and DL data qualities could impact lidar derived results. As indicated early, clouds could strongly attenuate lidar measurements to bias lidar derived results low. DL lidar signal-to-noise ratio (SNR) profile is strongly dependent on aerosol vertical distributions. There are cases that ML grows deeper, DL signals may not have enough SNR to cover the full range [40].

Fourth, atmospheric thermodynamics structures are not always consistent with atmospheric turbulence structures. In the absence of wind shear, PBL turbulence quickly dissipates near sunset, but potential temperature changes slowly after sunset until the stable surface layer develops [65]. Therefore, MLH derived from vertical velocity variance could be lower than the sounding results around sunset. In some extreme examples, when  $h_{RI}$  is still close to PBLH, the MLH derived from vertical velocity decreases near to the ground, but these extreme cases are not included in Fig. 9(b).

Considering these sources of uncertainties for both measurements, results in Fig. 9 indicated that PBLHs from RL WVMR and MLHs from DL vertical velocity measurements are reliable for model evaluations and process study.

### 5.2. Example of diurnal variations of PBLH and MLH

As discussed earlier, there is strong diurnal cycle of PBL structure over land. Therefore, PBLHs and MLHs provide a first order description of PBL diurnal variations. Figure 10 shows the PBLH and MLH evolutions of a typical clear sunny day at the SGP site. The night time PBL residual layer is about 1 km. After sunrise, ML started to develop at about 07:30 (local time). At about 09:30, the ML reaches the residual layer top, and PBLH and MLH are at the same height. Then, deepening ML pushes the PBL upward, PBLHs and MLHs evolve together from 10:00 to 18:30, which suggests that WVMR based PBLHs and vertical velocity based MLHs are consistent. The ML quickly dissipates after sunset (about 19:00), but PBL top slowly damps down. The MLH and PBLH are highly consistent with the bulk Richard method's height ( $RI = 0.25$ ) and consistent with the potential temperature's inflection point height. This example further highlights that DL and RL provide complement measurements for PBL characterization.

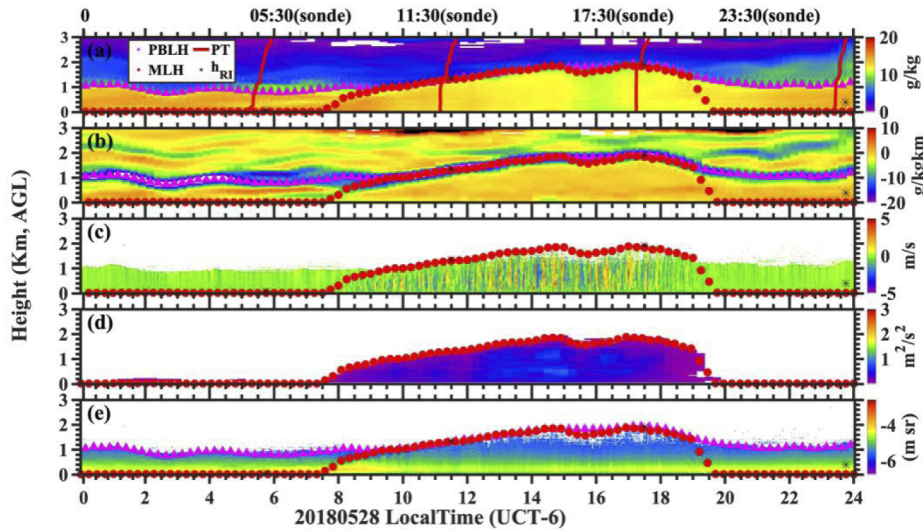


**Fig. 10.** Diurnal evolution of PBLHs and MLHs on May 28<sup>th</sup>, 2018: (a) RL WVMR, (b) slope of WVMR, (c) DL vertical wind velocity, (d) wavelet reconstructed vertical velocity variance, (e) DL aerosol backscattering coefficients. PBLHs and MLHs are over-plotted in above 2-D cross-sections.

### 5.3. Diurnal evolution of PBLH and MLH during the warm season

To capture warm season PBL variations, the algorithms are applied to five years (2016-2020) RL and DL observations at the SGP site from May 1<sup>st</sup> to October 1<sup>st</sup> (22 weeks). Quality controls are performed for each day. Then, we compose weekly averaged diurnal variations of PBLHs and MLHs and presented in Fig. 11. Data shown in Fig. 11 are from days when both Raman lidar data and doppler lidar data are available, and that day is not rainy.

Seasonal and diurnal variations of PBL structures in terms of PBLHs and MLHs are clearly displayed in Fig. 11. Daily ML developments are driven by solar radiations. Figure 11(a) shows that ML developments shift early from May to July and then gradually shift late as the sun moves to the southern hemisphere. ML deepens slowly in the morning, but dissipates quickly near sunset when the surface long wave energy loses outpace the absorbed solar energy. The overall turbulence is weak at night, leading to no ML and near zero MLH, but there are nights with detectable turbulence associated with the Low Level Jet [66] or wind shear. Furthermore, the mixing layer's highest value is between 14:00~16:00 in the afternoon, around the 12<sup>th</sup> to 14<sup>th</sup> week.

The diurnal variations of PBLHs are less significant than MLHs. Because nighttime residual layers are closely tied to the next daytime PBL developments, thus PBLH variations reflect accumulated effects. As illustrated in Fig. 11(c), PBLHs reach daily peaks as MLH peaks, but they gradually decrease during night and reach daily minimums around sunrise. Seasonally, PBLHs reach their highest in the 12<sup>th</sup> to 14<sup>th</sup> weeks (the Mid-late July to early August).

Besides these physically expected seasonal and diurnal variations, Figs. 11(a) and (c) show significant week-to-week jumps. Due to different cloudy and precipitation conditions, available samples for each week are different, which may attribute to some observed large week-to-week variabilities. There are also significant variations among sample days within a selected week. These PBLH and MLH variability during the same week and adjunct weeks indicate that multi-factors and complex processes control PBL evolutions beyond the surface energy forcing, which need to be better understood and represented in PBL parameterizations. At the SGP site,

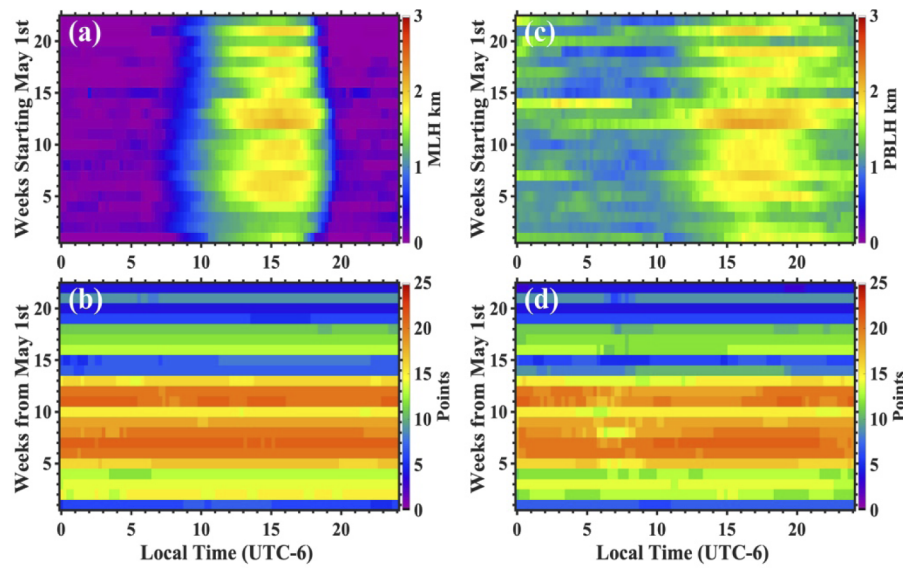


**Fig. 11.** The seasonal and diurnal evolutions of MLH and PBLH during the warm season based on weekly averages from May 1<sup>st</sup> to October 1<sup>st</sup>. (a) MLH variations, (b) PBLH variations, (c) weekly MLH sample points, (d) weekly PBLH sample points. The diurnal variations are represented along the x-axis with local time in 24 hours, and each horizontal line is a weekly mean. The seasonal variations are represented along the y-axis with 22 weekly means starting from May 1<sup>st</sup>.

there are many ancillary data available to support further process study as a part of our ongoing analysis.

We can see that our algorithms and statistical information can provide the basis for parameterization development and model performance evaluations through the above analysis.

## 6. Summary and conclusions

This article proposed new algorithms to provide reliable PBLH and MLH from RL and DL measurements to characterize the diurnal cycle of PBL in the warm season. For PBL height determination, we use RL water vapor measurements as a better trace than aerosols because lidar aerosol signals depend on both aerosol concentration and particle size. A new algorithm classifies PBL structure into several general patterns according to WVMR vertical distributions first, and then WVMR slopes to determine PBLH. For ML height determinations, we use DL vertical velocity measurements, which represent the vertical transport. The ML algorithm is designed to handle challenges associated with different size eddies and gravity waves in velocity variance calculations and the limitation of the fixed variance threshold approaches. The algorithm first uses wavelet results from vertical velocities at ~600 m AGL to identify days dominated by large-size eddies. Then the wavelet analysis is applied to all heights to reconstruct 2-D vertical velocity variance by selecting power spectrum within a sub-set frequency range according to the dominant eddy size. Finally, dynamic thresholds are applied to reconstruct the 2-D variance profile to determine MLH.

Remotely sensed PBLHs and MLHs are compared with radiosonde measurements based on the RI method. Good agreements between them confirm that the proposed new algorithms are reliable for PBLH and MLH characterizations. The consistency between WVMR derived PBLHs and vertical velocity derived MLHs after ML fully developed also indicated that WVMR derived

PBLHs are reliable. Thus, combining RL and DL measurements provide PBLHs and MLHs to characterize the diurnal evolutions of PBL.

The algorithms are applied to warm seasons RL and ML measurements for five years to study the warm season PBL structure and processes. The weekly composited diurnal evolutions of PBLHs and MLHs on warm climate were analyzed. The results showed that MLH and PBLH reached the highest value from mid-July to early August and they reach their peaks in mid-afternoon daily. The overall daily and seasonal evolution of PBLH and MLH is consistent with the earth's response to solar radiation. However, significant intraday variations indicate that factors other than solar radiation are also critical in controlling PBL developments. As a part of ongoing efforts, these measurements are used to understand processes controlling PBL variations.

It is important to note that the upper limit of MLH could be limited by DL lidar data quality. There are five DLs at the SGP super sites. The SNR profiles among these DL systems are significant differences in the upper PBL. For DL with poor data quality in upper PBL, especially under low aerosol loading conditions, under estimated MLH in afternoon is possible. Also, the lowest MLH height is limited by the lowest available DL measurements, which is at 75m for current DL systems at the SGP site. Another general limitation of using lidar measurements is that results are limited to periods without low level stratiform clouds (measurements between scattering cumulus can be used) and precipitation. For the process study, it is important to consider this sampling limitation. Combining microwave measurements are needed to cover all weather conditions.

Although there are limited combined RL and DL measurements available now, WVVMR and vertical velocity measurements will be inerasably available in the future. WVVMR from water vapor differential absorption lidars (DIAL) and DIAL systems with lower pulse energy lasers could be widely available for deployments for their lower cost. Furthermore, reliable PBLHs and MLHs from RL and DL measurements could be used as training and evaluation datasets for aerosol-based PBLH determination methods by taking advantage of other collocated micropulse lidar and ceilometer measurements at the SGP site.

A key motivation to use combined RL and DL measurements to provide reliable PBLH and MLHs is for PBL process study, model evolution, and PBL parameterization improvements. At the SGP site, comprehensive measurements, such as surface flux measurement network, radiation, and clouds, are available to understand PBL process controlling observed spatial temporal PBL variations. These observations are also used to evaluate LES and single column model simulations [67].

**Funding.** U.S. Department of Energy (DE-SC0020171); National Science Foundation (AGS 1917693); National Natural Science Foundation of China (41875033).

**Acknowledgments.** Data were obtained from the Atmospheric Radiation Measurement (ARM) user facility, a U.S. Department of Energy (DOE) office of science user facility managed by the biological and environmental research program. The authors acknowledge financial support from China Scholarship Council.

**Disclosures.** The authors declare no conflicts of interest

**Data availability.** Data underlying the results presented in this paper are available in Ref. [58].

## References

1. R.B. Stull, *An introduction to boundary layer meteorology*, (Kluwer Academic Publishers, 1988).
2. T.R. Oke, *Boundary Layer Climates*, (Halsted Press, 1988).
3. X.H. Lee, *Fundamentals of boundary layer meteorology*, (Springer, 2016).
4. J.R. Garratt, *Review: the atmospheric boundary layer*, (Elsevier, 1994).
5. M.A. Lemone, W.M. Angevine, C.S. Bretherton, F. Chen, J. Dudhia, E. Fedorovich, K.B. Katsaros, D.H. Lenschow, L. Mahrt, E.G. Patton, and J. Sun, "100 years of progress in boundary layer meteorology," *Meteorol Monogr*. **59**, 9.1–9.85 (2019).
6. P. Seibert, F. Beyrich, S. E. Gryning, S. Joffre, A. Rasmussen, and P. Tercier, "Review and intercomparison of operational methods for the determination of the mixing height," *Atmos. Environ.* **34**(7), 1001–1027 (2000).

7. S. Emeis, K. Schafer K, and C. Münker, "Surface-based remote sensing of the mixing-layer height – a review," *Meteorologische Zeitschrift* **17**(5), 621–630 (2008).
8. W.M. LeMone, W.M. Angevine, C.S. Bretherton, F. Chen, J. Dudhia, E. Fedorovich, K.B. Katsaros, D.H. Lenschow, L. Mahrt, E.G. Patton, and J. Sun, "Transition periods in the diurnally-varying atmospheric boundary layer over land," *Boundary-Layer Meteorol* **177**(2-3), 205–223 (2020).
9. H.H. Shin and J. Dudhia, "Evaluation of PBL parameterizations in WRF at sub kilometer grid spacings: Turbulence statistics in the dry convective boundary layer," *Mon. Weather Rev.* **144**(3), 1161–1177 (2016).
10. Y. Zhang, V. Duliére, P. W. Mote, and E. P. Salathé, "Evaluation of WRF and HadRM mesoscale climate simulations over the U.S. Pacific Northwest," *J. Clim.* **22**(20), 5511–5526 (2009).
11. J. Kyselý and E. Plavcová, "Biases in the diurnal temperature range in Central Europe in an ensemble of regional climate models and their possible causes," *Clim Dyn* **39**(6), 1275–1286 (2012).
12. X. Hu, J. Nielsen-Gammon, and F. Zhang, "Evaluation of Three Planetary Boundary Layer Schemes in the WRF Model," *J. Appl. Meteorol. Climatol.* **49**(9), 1831–1844 (2010).
13. A. Holtslag, G. Svensson, P. Baas, S. Basu, B. Beare, A.C. Beljaars, F.C. Bosveld, J. Cuxart, J. Lindvall, G.J. Steeneveld, M. Tjernström, and B.J. Van De Wiel, "Stable Atmospheric Boundary Layers and Diurnal Cycles: Challenges for Weather and Climate Models," *Bull. Am. Meteorol. Soc.* **94**(11), 1691–1706 (2013).
14. D. Seidel, Y. Zhang, A. Beljaars, J.C. Golaz, A. R. Jacobson, and B. Medeiros, "Climatology of the planetary boundary layer over the continental United States and Europe," *J. Geophys. Res.* **117**(D17), D17106 (2012).
15. A.E. Cohen, S. Cavallo, M. Coniglio, and H. Brooks, "A Review of Planetary Boundary Layer Parameterization Schemes and Their Sensitivity in Simulating Southeastern US Cold Season Severe Weather Environments," *Mon. Weather Rev.* **30**(3), 591–612 (2015).
16. G. Bryan and H. Morrison, "Sensitivity of assimilated squall line to horizontal resolution and parameterization of microphysics," *Mon. Wea. Rev.* **140**(1), 202–225 (2012).
17. R. Honnert, V. Masson, and F. Couvreux, "A diagnostic for evaluating the representation of turbulence in atmospheric models at the kilometric scale," *J. Atmos. Sci.* **68**(12), 3112–3131 (2011).
18. H.H. Shin and S.Y. Hong, "Analysis of resolved and parameterized vertical transports in convective boundary layers at gray-zone resolutions," *J. Atmos. Sci.* **70**(10), 3248–3261 (2013).
19. Z. Janjic, "The step-mountain eta coordinate model: further developments of the convection, vicious sublayer, and turbulence closure schemes," *Mon. Weather Rev.* **122**(5), 927–945 (1994).
20. C. Bretherton and S. Park, "A new moist turbulence parameterization in the community atmosphere model," *J. Clim.* **22**(12), 3422–3448 (2009).
21. A.J. Clark, M.C. Coniglio, B.E. Coffey, G. Thompson, M. Xue, and F.Y. Kong, "Sensitivity of 24-h Forecast Dryline Position and Structure to Boundary Layer Parameterizations in Convection-Allowing WRF Model Simulations," *Weather and Forecasting* **30**(3), 613–638 (2015).
22. M. García-Díez, J. Fernández, L. Fita, and C. Yagüe, "Seasonal dependence of WRF model biases and sensitivity to PBL schemes over Europe," *Q. J. R. Meteorol. Soc.* **139**(671), 501–514 (2013).
23. D. Camuffo, C. Coceo, and S. Enzi, "Seasonality of instability phenomena (hailstorms and thunderstorms) in Padova, northern Italy, from archive and instrumental sources since AD 1300," *The Holocene* **10**(5), 635–642 (2000).
24. D. Wu, Z. Wang, P. Wechsler, N. Mahon, M. Deng, B. Glover, M. Burkhardt, W. Kuestner, and B. Heesen, "Airborne compact rotational Raman lidar for temperature measurement," *Opt. Express* **24**(18), A1210–1223 (2016).
25. R. Dang, Y. Yang, X. Hu, Z. Wang, and S. Zhang, "A Review of Techniques for Diagnosing the Atmospheric Boundary Layer Height (ABLH) Using Aerosol Lidar Data," *Remote Sensing* **11**(13), 1590 (2019).
26. V. Wolfmeyer and D. Turner, Land-Atmosphere Feedback Experiment Field Campaign Report (No. DOE/SC-ARM-18-007), DOE Office of Science Atmospheric Radiation Measurement (ARM) Program (United States, 2018).
27. C. Sivaraman, S. McFarlane, E. Chapman, M. Jensen, T. Toto, S. Liu, and M. Fischer, "Planetary boundary layer (PBL) height value added product (VAP): Radiosonde retrievals," *Department of Energy Office of Science Atmospheric Radiation Measurement (ARM) Program* (United States, 2013).
28. W. H. Moores, S.J. Caughey, C.J. Readings, J.R. Milford, D.A. Mansfield, S. Abdulla, T.H. Guymer, and W.B. Johnston, "Measurements of boundary layer structure and development over SE England using aircraft and tethered balloon instrumentation," *Q. J. R. Meteorol. Soc.* **105**(444), 397–421 (1979).
29. S. Benjamin, B. Schwartz, and R. Cole, "Accuracy of ACARS wind and temperature observations determined by collocation," *Mon. Weather Rev.* **14**(6), 1032–1038 (1999).
30. A.B. White, C.W. Fairall, and D.W. Thomson, "Radar Observations of Humidity Variability in and above the Marine Atmospheric Boundary Layer," *J. Atmos. Oceanic Technol.* **8**(5), 639–658 (1991).
31. F. Beyrich, "On the use of SODAR data to estimate mixing height," *Appl. Phys. B: Photophys. Laser Chem.* **57**(1), 27–35 (1993).
32. R. Collis, "Lidar: a new atmospheric probe," *Q. J. R. Meteorol. Soc.* **92**(392), 220–230 (1966).
33. S. H. Melfi, J.D. Spinhirne, S.H. Chou, and S.P. Palm, "Lidar Observations of Vertically Organized Convection in the Planetary Boundary Layer over the Ocean," *J. Clim. Appl. Meteorol.* **24**(8), 806–821 (1985).
34. M. Frioud, V. Mitev, R. Matthey, C.H. Häberli, H. Richner, R. Werner, and S. Vogt, "Elevated aerosol stratification above the Rhine Valley under strong anticyclonic conditions," *Atmos. Environ.* **37**(13), 1785–1797 (2003).

35. L. Menut, C. Flamant, J. Pelon, and P.H. Flamant, "Urban boundary-layer height determination from lidar measurements over the Paris area," *Appl. Opt.* **38**(6), 945–954 (1999).
36. D. G. Steyn, M. Baldi, and R. M. Hoff, "The Detection of Mixed Layer Depth and Entrainment Zone Thickness from Lidar Backscatter Profiles," *J. Atmos. Oceanic Technol.* **16**(7), 953–959 (1999).
37. W. Wang, W. Gong, F. Mao, and Z. Pan, "An Improved Iterative Fitting Method to Estimate Nocturnal Residual Layer Height," *Atmosphere* **7**(8), 106 (2016).
38. I.M. Brooks, "Finding Boundary Layer Top: Application of a Wavelet Covariance Transform to Lidar Backscatter Profiles," *J. Atmos. Oceanic Technol.* **20**(8), 1092–1105 (2003).
39. A.K. Piironen and E.W. Eloranta, "Convective boundary layer mean depths and cloud geometrical properties obtained from volume imaging lidar data," *J. Geophys. Res.* **100**(D12), 25569–25576 (1995).
40. R. Krishnamurthy, R.K. Newsom, L.K. Berg, H. Xiao, P.L. Ma, and D.D. Turner, "On the estimation of boundary layer heights: a machine learning approach," *Atmos. Meas. Tech.* **14**(6), 4403–4424 (2021).
41. T. Luo, R. Yuan, and Z. Wang, "Lidar Based Remote Sensing of Atmospheric Boundary Layer Height Over Land and Ocean," *Atmos. Meas. Tech.* **7**(1), 173–182 (2014).
42. Taniguchi, Kyoko: Characterization of Water Vapor within the Planetary Boundary Layer Based on the ARM Raman Lidar Observation at the SGP Site, M.S. thesis, Department of Atmospheric Science, University of Wyoming August, 2007.
43. A. Pantazis, A. Papayannis, and G. Georgios, "Lidar algorithms in 3D scanning for atmospheric layering and planetary boundary layer height retrieval: comparison with other techniques," *Opt. Express* **57**(28), 8199–8211 (2018).
44. R. Newsom and K. Raglavendra, Doppler Lidar (DL) instrument handbook. No. DOE/SC-ARM/TR-101, DOE Office of Science Atmospheric Radiation Measurement (ARM) user facility (2020).
45. M. de Bruine, A. Apituley, D.P. Donovan, H. K. Baltink, and M. J. de Hajj, "Pathfinder: applying graph theory to consistent tracking of daytime mixed layer height with backscatter lidar," *Atmos. Meas. Tech.* **10**(5), 1893–1909 (2017).
46. Y. Pan, Z. Jin, P. Tong, W. Xu, and W. Wang, "Edge Detection Method for Determining Boundary Layer Height Based on Doppler Lidar," *Atmosphere* **12**(9), 1103 (2021).
47. K. Patel, J. Sleeman, and M. Haleem, "Physics-aware deep edge detection network," *Proc. SPIE 11859, Remote Sensing of Clouds and the Atmosphere XXVI*, 1185908 (12 September 2021).
48. R. Thomas, A. Sylvain, and M. Tiago, "Mixing height derivation from aerosol lidar using machine learning: KABL and ADABL algorithms," *Atmos. Meas. Tech.* **78**, 78 (2020).
49. G. Taylor, "Statistical theory of turbulence part I–IV," *Proceedings of the London Mathematical Society* **151**, 421–478 (1935).
50. S.C. Tucker, C.J. Senff, A.M. Weickmann, W.A. Brewer, R.M. Banta, S.P. Sandberg, D.C. Law, and R.M. Hardesty, "Doppler Lidar Estimation of Mixing Height Using Turbulence, Shear, and Aerosol Profiles," *J. Atmos. Oceanic Technol.* **26**(4), 673–688 (2009).
51. G. Pearson, F. Davies, and G. Collier, "Remote sensing of the tropical rain forest boundary layer using pulsed Doppler lidar," *Atmos. Chem. Phys.* **10**(13), 5891–5901 (2010).
52. J. F. Barlow, T.M. Dunbar, E.G. Nemitz, C.R. Wood, M.W. Gallagher, F. Davies, E. O'Connor, and R.M. Harrison, "Boundary layer dynamics over London, UK, as observed using Doppler lidar during REPARTEE-II," *Atmos. Chem. Phys.* **11**(5), 2111–2125 (2011).
53. V. Vakkari, E.J. O'Connor, A. Nisantzi, R.E. Mamouri, and D.G. Hadjimitsis, "Low-level mixing height detection in coastal locations with a scanning doppler lidar," *Atmos. Meas. Tech.* **8**(4), 1875–1885 (2015).
54. K. Träumner, C. Kottmeier, U. Corsmeier, and A. Wieser, "Convective Boundary-Layer Entrainment: Short Review and Progress using Doppler Lidar," *Boundary-Layer Meteorol* **141**(3), 369–391 (2011).
55. M. Jia, J. Yuan, C. Wang, H. Xia, Y. Wu, L. Zhao, T. Wei, J. Wu, L. Wang, S. Gu, and L. Liu, "Long-lived high-frequency gravity waves in the atmospheric boundary layer: observations and simulations," *Atmos. Chem. Phys.* **19**(24), 15431–15446 (2019).
56. V. Banakh, I. Smalikh, and A. Falits, "Estimation of the height of the turbulent mixing layer from data of Doppler lidar measurements using conical scanning by a probe beam," *Atmos. Meas. Tech.* **14**(2), 1511–1524 (2021).
57. J. Mather and J. Voyles, "The ARM Climate Research Facility: A review of structure and capabilities," *Bull. Am. Meteorol. Soc.* **94**(3), 377–392 (2013).
58. "Atmospheric Radiation Measurement (ARM) Climate Research Facility Management Plan DOE/SC-ARM-13-022," U.S. Department of Energy (2016).
59. D.L. Sisterson, R.A. Pepple, T.S. Cress, P.J. Lamb, and D.D. Turner, "The ARM Southern Great Plains (SGP) Site," *Meteorological Monographs* **57**, 6.1–6.14 (2016).
60. R.K. Newsom, "Raman Lidar (RL) Handbook," Office of Scientific & Technical Information Technical Reports (2009).
61. C. Torrence and G.P. Compo, "A Practical Guide to Wavelet Analysis," *Bull. Am. Meteorol. Soc.* **79**(1), 61–78 (1998).
62. S. Liu and X. Liang, "Observed Diurnal Cycle Climatology of Planetary Boundary Layer Height," *J. Clim.* **23**(21), 5790–5809 (2010).
63. D. Seidel, B. Sun, and M. Pettey, "Global radiosonde balloon drift statistics," *J. Geophys. Res.* **116**(D7), D7 (2014).

64. Y. zhang, Z. Gao, and D. Li, "On the computation of planetary boundary-layer height using the bulk Richardson number method," *Geoscientific Model Development*. **7**(6), 4045–4079 (2014).
65. U. Rizza, M. M. Miglietta, G. A. Degrazia, O. C. Acevedo, and E. P. Marques Filho, "Sunset decay of the convective turbulence with Large-Eddy Simulation under realistic conditions," *Phys. A (Amsterdam, Neth.)* **392**(19), 4481–4490 (2013).
66. D. Burrows, C. Ferguson, M. Campbell, X. Geng, and L.F. Bosart, "An Objective Classification and Analysis of Upper-Level Coupling to the Great Plains Low-Level Jet over the Twentieth Century," *J. Clim.* **32**(21), 7127–7152 (2019).
67. H.H. Shin, L. Xue, W. Li, G. Firl, D.F. D'Amico, D. Muñoz-Esparza, M.B. Ek, Y. Chu, Z. Wang, W.I. Gustafson Jr, and A.M. Vogelmann, "Large-Scale Forcing Impact on the Development of Shallow Convective Clouds Revealed from LASSO Large-Eddy Simulations," *JGR Atmospheres* **126**(20), 2021JD035208 (2021).